Materials Horizons

ROYAL SOCIETY OF CHEMISTRY

COMMUNICATION

View Article Online
View Journal | View Issue

Cite this: *Mater. Horiz.*, 2025, **12**, 3907

Received 10th December 2024,
Accepted 7th March 2025

DOI: 10.1039/d4mh01804d

rsc.li/materials-horizons

Development of novel multi-responsive 4D printed smart nanocomposites with polypyrrole coated iron oxides for remote and adaptive transformation†

Shengbo Guo,[a] Tarun Agarwal,[a] Shuaiqi Song,[a] Kausik Sarkar[a] and Lijie Grace Zhang *[abcd]

Four-dimensional (4D) printing, a state-of-the-art additive manufacturing technology, enables the creation of objects capable of changing shape, properties, or functionality over time in response to external stimuli. However, the lack of effective remote control and reliance on a single actuation method pose significant challenges, limiting its applications in various fields. This study aims to address these limitations by developing a novel multi-responsive nanocomposite. By coating near-infrared light (NIR)-responsive polypyrrole (PPy) onto the surface of magnetic iron oxide (Fe_2O_3) nanoparticles (NPs), multi-responsive PPy@Fe_2O_3 NPs were synthesized. Doping PPy@Fe_2O_3 into a thermo-responsive shape memory polymer (SMP) matrix created a nanocomposite with excellent NIR and magnetic responsiveness, enabling dynamic, remote-controlled shape transformation of printed objects with precise timing and positioning using NIR and a magnetic field. Using the nanocomposite, a proof-of-concept semi-tubular construct was fabricated to evaluate its controllable transformation capability and assess the potential for modulating neural stem cell (NSC) behaviors. Furthermore, three proof-of-concept smart robots with distinct features were designed and fabricated for cargo delivery in diverse scenarios and different purposes. Importantly, all complex operations of these robots were remotely controlled using NIR illumination and an external magnetic field. This novel approach demonstrates significant progress in addressing the key challenges of remote control and actuation in 4D printing, highlighting its potential for enhanced versatility and functionality across various applications.

New concepts

This study introduces a multi-functional 4D-printed smart nanocomposite that integrates near-infrared responsiveness and magnetic properties with a thermo-responsive shape memory polymer matrix. This unique combination enables dynamic, remote-controlled transformations with high precision and spatiotemporal adaptability. Unlike conventional 4D materials relying on single stimuli, this multi-responsive system supports diverse applications, including intricate robotic manipulation, precise cargo delivery, and programmable biomedical scaffolds. By demonstrating precise transformations and multi-tasking capabilities, this innovative concept broadens the horizons of smart materials for biorobotics and biomedicine.

Introduction

Emerging as a state-of-the-art technology, four-dimensional (4D) printing incorporates external stimuli-induced transformations into the design of smart materials and structures, enabling printed constructs to be reprogrammed in form or function.[1,2] Beyond simply introducing "time" as the fourth dimension, 4D printing significantly broadens the applications of additive manufacturing across various fields. For instance, in biomedicine, 4D printing holds enormous potential for fabricating smart bioengineering structures that mimic dynamic tissue environments and facilitate the creation of complex, adaptive structures for precise tissue implantation.[2,3] Moreover, 4D printing has established an innovative platform for developing micromachines for various applications, such as minimally invasive surgical devices and smart drug delivery systems.[2,4,5]

Currently, thermo-responsive shape memory polymers (SMPs) are one of the most extensively used smart materials in 4D printing. The 4D transformation of SMPs is primarily driven by changes in the physicochemical properties induced by temperature change.[2,6] Taking thermoset SMPs as an example, the shape memory effect is primarily due to the phase transition between the glassy and rubbery states. This transition occurs

[a] *Department of Mechanical and Aerospace Engineering, The George Washington University, Washington, DC, 20052, USA. E-mail: lgzhang@gwu.edu*
[b] *Department of Electrical Engineering, The George Washington University, Washington, DC, 20052, USA*
[c] *Department of Biomedical Engineering, The George Washington University, Washington, DC, 20052, USA*
[d] *Department of Medicine, The George Washington University, Washington, DC, 20052, USA*
† Electronic supplementary information (ESI) available. See DOI: https://doi.org/10.1039/d4mh01804d

when the material is heated above its glass transition temperature (T_g), deformed, and then cooled, storing elastic energy in a frozen state that can be recovered by reheating the material.[7,8] Building on this mechanism, Miao *et al.* fabricated a 4D cell culture substrate using epoxy-based SMPs, whose self-morphing transition is induced by temperature at 37 °C, enabling the modulation of neural stem cell (NSC) differentiation.[9] However, as a triggering method for 4D transformation, thermal actuation has obvious limitations. For example, commonly used methods such as water baths, heat guns, or hot plates require direct contact between the construct and the heat source.[9–11] Additionally, the contact area between the construct and the stimulus cannot be precisely controlled, resulting in an uncontrollable transformation process.

To address this challenge, researchers have been exploring diverse stimuli for triggering 4D transformation. Among these approaches, the incorporation of nanomaterials has proven to be an effective strategy for developing smart materials capable of responding to stimuli beyond thermal actuation in 4D printing.[5] For example, doping photothermal nanomaterials into a thermo-sensitive SMP matrix enables light-to-heat conversion, providing an effective approach for developing light-responsive smart materials. Using this strategy, Yang *et al.* developed a photosensitive material by incorporating carbon black into polyurethane, enabling its 4D-printed construct to undergo shape transformations triggered by simulated solar light or natural sunlight.[12] In addition to introducing new responsiveness, functional nanomaterials can also endow smart materials with novel properties. For instance, by immersing a smart hydrogel in a suspension of magnetic Fe_3O_4 nanoparticles (NPs), Xin *et al.* developed a smart hydrogel with magnetic properties, which was then used to fabricate 4D-printed microrobots capable of movement driven by an external magnetic field.[13] While current research has made significant progress in remote control, most studies still focus on single-stimulus-driven 4D transformations, with limited advancements in developing multi-responsive materials. In real-world applications, single-stimulus-driven 4D transformations often fall short of meeting complex practical demands. For instance, in microrobotics, an ideal system would allow not only remote control over movement but also precise regulation of actions such as grasping, lifting, and releasing. A fully remote-controlled approach enhances operational flexibility, minimizes the need for direct human intervention, and enables seamless functionality in constrained or hazardous environments.

To address the challenges of remote control and multifunctionality in 4D-printed smart structures, this study developed a novel multi-responsive nanocomposite with thermo-responsiveness, NIR-responsiveness, and magnetic properties. This material enables precise dynamic control over the shape transformation process, allowing for spatiotemporal precision, quick actuation, and magnetically driven remote controllability. This was achieved by incorporating synthesized polypyrrole (PPy)-coated Fe_2O_3 NPs—PPy@Fe_2O_3 NPs, which provide both NIR-responsiveness and magnetic functionality, into a thermo-responsive SMP matrix. Leveraging this nanocomposite, a series of 4D-printed magnetic smart robots were fabricated, capable of performing complex NIR-induced tasks such as cargo gripping, transporting, and controllable release in specific locations. Examples include a smart gripper, a smart crab, and a smart star, each designed for various applications. This nanocomposite and the resulting smart robots are expected to serve as a versatile platform for advancing biomedical research, enhancing cell transport efficiency, and enabling more precise disease treatments.

Results and discussion

The 4D nanocomposite is primarily composed of a thermo-responsive SMP matrix and synthesized PPy@Fe_2O_3 NPs (Fig. 1a). The SMP formulation consists of three key components: bisphenol A diglycidyl ether (BDE, B), a rigid epoxy monomer; poly(propylene glycol)bis(2-aminopropyl)ether (PBE, P), a flexible aliphatic crosslinker; and decylamine (DA, D), a crosslinking modulator. Together, these components combine to create the SMP matrix, referred to as the neat epoxy ink, denoted as BPD based on the initials of each component. Building on a previous study from our lab, the ink was formulated using molar ratios of BDE, PBE, and DA at 1 : 0.275 : 0.45, respectively, represented as BP275D450.[9] This specific formulation was selected for its T_g, which is slightly above 37 °C, ensuring effective shape fixation at cell culture temperature (Table S1, ESI†). Multifunctional PPy@Fe_2O_3 NPs were synthesized by coating Fe_2O_3 NPs with photothermal PPy through oxidative polymerization of pyrrole. Fig. 1b and Fig. S1, ESI† show the Fourier transform infrared (FTIR) spectra of the pure PPy, pure Fe_2O_3 NPs and synthesized PPy@Fe_2O_3 NPs. Characteristic peaks for PPy are observed in its spectrum, confirming the formation of PPy. The peaks at 1534.09 cm^{-1} and 1448.63 cm^{-1} are attributed to C=C and C–N stretching vibrations in PPy, respectively. In the FTIR spectrum of Fe_2O_3 NPs, the peak at 537.45 cm^{-1} is associated with Fe–O stretching vibrations, while the peak at 415.97 cm^{-1} corresponds to Fe–O bending vibrations. The FTIR spectrum of PPy@Fe_2O_3 NPs demonstrates the presence of both PPy and Fe_2O_3, confirmed by the new peaks at 1540.19 cm^{-1} and 1457.50 cm^{-1}, as well as 524.01 cm^{-1} and 416.20 cm^{-1}, respectively. Besides, as the component that imparts multifunctionality to the nanocomposite, PPy@Fe_2O_3 NPs exhibited dual functionalities – photothermal effects and magnetic properties (Fig. S2, ESI†). More specifically, PPy was selected for its excellent photothermal performance, while Fe_2O_3 was chosen to provide the NPs with magnetic properties.[14,15] The PPy@Fe_2O_3 NPs were dispersed into BP275D450, at concentrations of 0%, 2.5%, 5%, 10%, and 15%, and the samples were represented as S0, S2.5, S5, S10, and S15, respectively. The S0 sample was taken as a control for the study. Due to the combined effects of van der Waals forces, π–π stacking, and hydrogen bonding between the aromatic epoxy resin and the dispersed PPy@Fe_2O_3 NPs, the PPy@Fe_2O_3 NPs were homogeneously dispersed in the ink, transforming the initially transparent ink into a black color.[16,17] Post-formulation, the 4D inks were extruded into a replica mold and then thermally cured at 70 °C. During the curing process, the epoxy group of BDE reacts with the amino functional group of PBE,

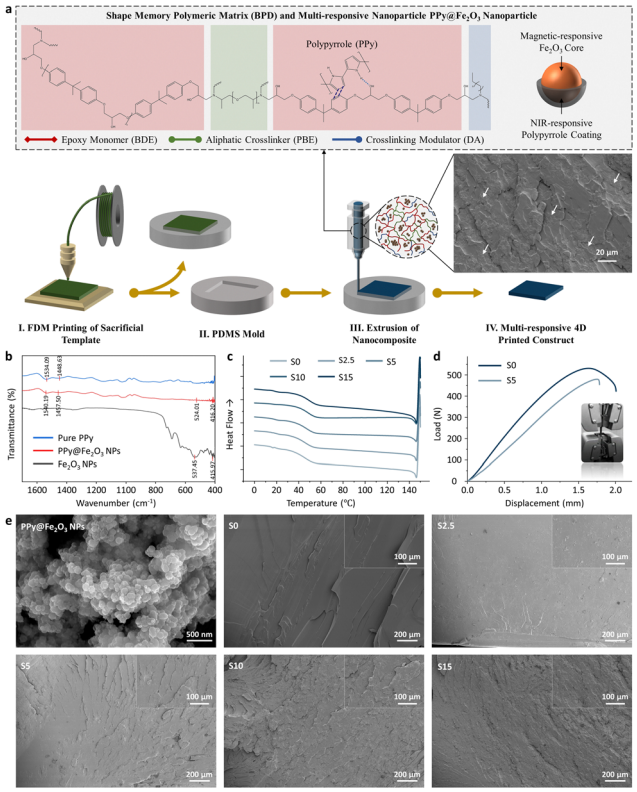

Fig. 1 Synthesis, fabrication, and characterization of 4D nanocomposite inks. (a) Chemical composition of the nanocomposite ink, comprising a thermo-responsive shape memory polymeric matrix integrated with synthesized dual-functional PPy@Fe_2O_3 NPs. Dual printing techniques—fused deposition modeling (FDM) and ink extrusion were developed for the fabrication of the nanocomposite. The SEM image shows the cross-section of the nanocomposite (S15), the arrow indicates the PPy@Fe_2O_3 NPs within the structure. (b) FT-IR spectra of pure PPy without Fe_2O_3 NPs, synthesized PPy@Fe_2O_3 NPs, and as-received Fe_2O_3 NPs. (c) DSC analysis of the pure SMP and nanocomposite, indicating a comparable T_g of approximately 45 °C across the samples. The arrow indicates the endothermic process. (d) Load-extension curves of specimens prepared from pure SMP and nanocomposite containing 5% PPy@Fe_2O_3 NPs, respectively. The mechanical characterization of all specimens was conducted at room temperature through uniaxial tensile testing. (e) SEM image of PPy@Fe_2O_3 NPs, and cross-section of pure SMP and different nanocomposite constructs. The inset images show enlarged views of the morphologies.

creating a network structure.[18] More specifically, the lone pair of electrons on the amine nitrogen attacks the electrophilic carbon in the epoxy ring, forming a secondary amine and hydroxyl group, which can further react with another epoxy group to form a tertiary amine, creating a cross-linked polymer network.[19,20] In the reaction, the amino group from decylamine reacts with the epoxy group, blocking network formation and modulating the shape memory properties of the SMP. All the final cured constructs were solid and relatively rigid. The constructs with NPs appeared black while the control set appeared pale yellowish with a smooth surface. Cross-sectional images of all nanocomposite samples displayed a uniform distribution of NPs at the macroscale (Fig. S3, ESI†). However, higher-magnification SEM analysis (Fig. 1a) revealed that, while the NPs were generally well-dispersed throughout the matrix, they also exhibited a tendency to form clusters. Besides, all nanocomposite samples exhibited magnetic properties. The constructs were subsequently subjected to physicochemical characterizations.

In 4D printing, the T_g value is crucial as it not only controls shape transformation (fixation and recovery) but also ensures stability and performance in specific applications. Thus, a DSC analysis was conducted to evaluate the T_g values of the samples (Fig. 1c). The results demonstrate that as the NP content increased, the T_g of the nanocomposites slightly increased, with T_g values of S0, S2.5, S5, S10, and S15 being 44.65, 44.73, 46.19, 47.86, and 48.39 °C, respectively. The observed change in T_g is attributed to the restricted mobility of SMP chains at the molecular level due to an increase in their interaction with the NPs. As a result, the nanocomposite requires greater heat input to transition from the glassy to the rubbery state, thereby shifting its T_g to higher temperatures.[21] Besides, no melting peak was observed from 0 to 140 °C, indicating that the samples were highly cross-linked and had no crystalline domains, as also reported by Cui *et al.*[22] The mechanical properties of SMPs also affect their ability to deform, recover, and endure external forces during 4D transformation.[23] To characterize the mechanical performance of the nanocomposites, uniaxial tensile testing was conducted at room temperature, and the results are shown in Fig. 1d and Fig. S4, ESI.† Compared to pure epoxy (S0), the nanocomposites (S5) demonstrated reduced ductility and tensile modulus. This observed change in mechanical properties is likely due to alterations in polymeric arrangement caused by the addition of PPy@Fe_2O_3 NPs. As shown in the scanning electron microscopy (SEM) images in Fig. 1e, the synthesized PPy@Fe_2O_3 NPs exhibit as discrete spherical morphology with a uniform size distribution. Based on measurements, the average nanoparticle diameter is approximately 118.72 ± 11.93 nm (mean ± standard deviation, n = 20). Energy-dispersive X-ray (EDX) spectroscopy analysis (Fig. S5, ESI†) confirmed the presence of C, N, O, and Fe, suggesting the successful synthesis of PPy@Fe_2O_3 NPs. Elemental mapping (Fig. S5, ESI†) showed a uniform distribution of Fe and O across the field of view taken. Besides, the cross-sectional view of S0 revealed a smooth internal structure, whereas samples S2.5–S15 displayed lamellar microstructures, with increasing roughness corresponding to higher PPy@Fe_2O_3 NP content. These variations in microstructure likely contributed to the significant differences in mechanical moduli among the samples. This finding aligns with previous studies, which have demonstrated a correlation between filler-induced microstructural changes and variations in mechanical properties.[22]

Chemically, the permanent (original) shape of an SMP structure is defined by the cross-links, while the transition to a temporary (programmed) shape is determined by the switching segments, which are activated by the transition temperature (T_{trans}), typically denoted as the T_g. A typical SMP is rigid and resistant to bending in its glass phase (below T_g). However, when the temperature exceeds T_g, it transitions into a soft and malleable rubber phase. This reversible transition between glassy and rubbery states enables the sequential shape memory cycle.

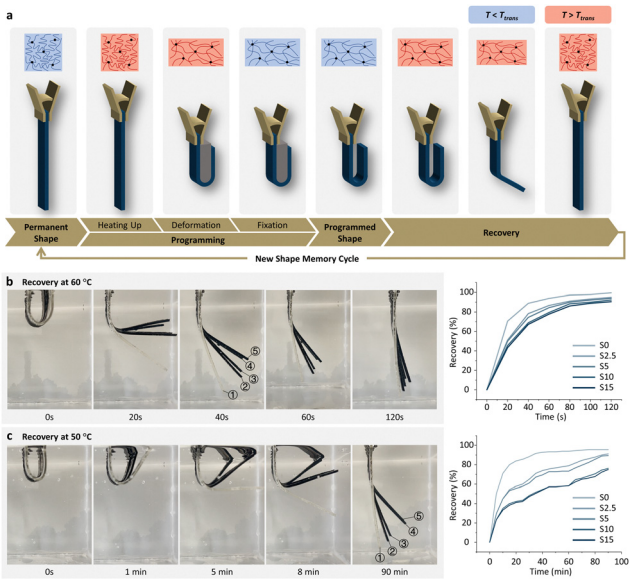

Fig. 2 Thermo-triggered shape memory properties of nanocomposite constructs. (a) A typical thermo-triggered shape memory cycle involves heating the SMP, initially in its permanent shape, above its T_g, allowing it to deform into a temporary shape under external stress. Cooling below T_g fixes the temporary shape, and upon reheating above T_g, the construct returns to its original shape. (b) and (c) The thermo-triggered shape memory behaviors of stripe samples from S0 to S15 at 60 °C and 50 °C, respectively, followed by the corresponding dynamic recovery processes, are illustrated by the correlation between recovery ratio and incubation time.

Fig. 2a illustrates a typical thermosensitive shape memory cycle of thermoset SMPs: when an SMP is heated above its T_g, the molecular switching segments in its polymer network "soften," allowing deformation to create a temporary shape under external stress; upon cooling below T_g, the predesigned temporary shape is fixed as the molecular switching segments "freeze", trapping entropic energy within the polymer chains; reheating above T_g softens the segments again, and the stored entropic energy drives the structure to revert to its original shape, completing the shape memory cycle.[24] In our study, all the samples (strips) were fixed into a temporary "U-shape" by exposing them at 60 °C ($>T_g$) for deformation followed by 0 °C ($<T_g$) for shape fixation. All the samples (S0–S15) exhibited an excellent R_f of ~99%. Further, when subjected to a 60 °C water bath (Fig. 2b), all samples recovered to permanent shape within 120 seconds, with S0 recovering faster than the nanocomposite samples (S2.5–S15). When compared to S0 (R_r ~96%), the addition of NPs negatively affected the shape recovery behavior, with lower R_r values of ~94%, 92%, 91%, and 90% observed in S2.5 to S15 samples at 60 °C, respectively. This could be attributed to the fact that the predominant interaction forces between the NPs and the SMP matrix are primarily van der Waals forces, which intensify as the NP content increases. When these forces exceed the deformation energy required for shape recovery, they negatively affect both the shape recovery time and the recovery ratio.[25] Additionally, the long-term shape memory performance of the samples (S0–S15) was evaluated through a 10-cycle shape memory test at 60 °C to assess their repeatability and durability. The results indicate that even after 10 shape memory cycles, all samples maintained a R_r above 95% (Fig. S6, ESI†). Lowering the triggering temperature to 50 °C further slowed the recovery speed of all the samples, but the overall recovery pattern remained consistent (Fig. 2c). The increase in transformation time at lower triggering temperature was attributed to decreased kinetic energy of molecular chains, which limit their movement, resulting in a slower transition from the deformed to the original state.[26] Interestingly, samples also exhibited shape recovery at physiological human body temperature (37 °C); however, none of the samples (S0, S2.5, S5, S10, and S15) could recover completely in 15 days (Fig. S7, ESI†).

In this study, the PPy@Fe_2O_3 NPs within the nanocomposite functioned as photothermal agents, with the PPy coating exhibiting strong NIR absorption and converting photon energy into heat *via* lattice relaxation.[14,27] Under NIR illumination, the heat generated by PPy@Fe_2O_3 NPs within the nanocomposite effectively triggered the shape transformation of the thermo-responsive SMP matrix, enabling NIR-induced shape recovery through localized heating. Importantly, as illustrated in Fig. 3a, the NIR-triggered 4D transformation allows precise remote control over both the spatial selectivity and temporal regulation of shape change – capacities difficult to achieve with conventional thermo-triggered methods.[28] As shown in Fig. 3b, the S0 sample, which lacks PPy@Fe_2O_3 NPs, exhibited no NIR-triggered shape memory behavior, even after 5 minutes of exposure to NIR intensities of 1000 and 2000 mW. In contrast, Fig. 3c demonstrates that under high-intensity NIR illumination (2000 mW), all nanocomposite samples rapidly recovered to 90° within 25 seconds, with only minimal differences in recovery speeds. This rapid shape recovery can be attributed to the swift increase in local temperature under high-intensity NIR irradiation, quickly surpassing T_g and triggering fast shape recovery of the constructs. The nanocomposites with higher nanoparticle content (S10 and S15) exhibited higher saturation temperatures of approximately 140 °C and 145 °C, respectively, compared to the samples with lower nanoparticle content (S2.5 and S5), which had saturation temperatures of approximately 132 °C and 133 °C, respectively (Fig. S8, ESI†). On a similar ground, a reduction in NIR intensity to 1000 mW delayed the recovery process with nanocomposites (S2.5, S5, S10, and S15) reaching 90° at the endpoint in 120 s, 110 s, 101 s, and 91 s, respectively (Fig. S9, ESI†). This demonstrates the concentration-dependent shape recovery property of the nanocomposite. Further, to demonstrate the NIR transformation behavior, we selected the nanocomposite with a 5% content of PPy@Fe_2O_3 NPs due to its efficient photothermal and magnetic effects for further experiments, and 4D printed typical models–cherry blossoms, butterflies, and a human. Different from uncontrollable transformation in a thermo-triggered 4D changing process, a step-by-step precise remote control can be achieved with our 4D nanocomposite using this strategy (Fig. 3d and Movies S1–S3, ESI†). For example, in the human model undergoing 4D transformation, each limb

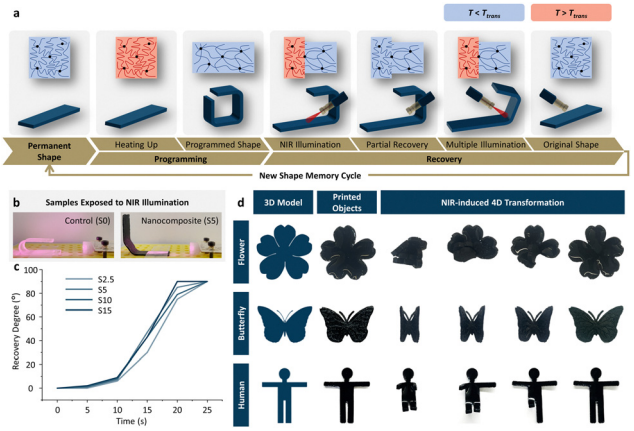

Fig. 3 Precisely and dynamically controllable NIR-triggered 4D transformation of nanocomposite. (a) Schematic of an NIR-triggered shape memory cycle. The printed nanocomposite construct has its permanent shape or original shape. After heating up, either by NIR illumination or direct thermal treatment, it can be softened and deformed by external force, and then the construct is fixed by quenching in ice water. This process is called programming. Upon NIR illumination, the constructs are heated to their T_g, resulting in the temporary shape returning to their original shapes gradually. By applying NIR to a specific area, dynamically and remotely controllable transformations can be achieved in a step-by-step and spatiotemporal manner. (b) The homemade devices used for NIR-triggered 4D transformation testing, and compared to the nanocomposite doped with PPy@Fe_2O_3 NPs, no photo-triggered shape memory behavior was observed in the pure SMP stripe. (c) The photo-triggered shape memory behavior of the nanocomposite constructs at an NIR intensity of 2000 mW. (d) NIR-triggered 4D transformation behavior of the nanocomposite models, including a cherry blossom blooming, a butterfly, and an exerciser. The shape of these models could be dynamically and precisely controlled under NIR exposure.

extended sequentially under NIR illumination without interference with each other, demonstrating the precision of controllable transformation.

To deepen our understanding of the theoretical foundation of controllable localized transformation, we examine the physical thermal properties of the nanocomposite. As expected, the incorporation of nanoparticles enhances the material's thermal conductivity and diffusivity. However, despite this improvement, the nanocomposite still exhibits relatively low thermal conductivity and diffusivity (Fig. S10 and Table S2, ESI†).[29–31] For example, the thermal conductivity and diffusivity of S5 are approximately 1.34 W m^{-1} K^{-1} and 6.42 × 10^{-4} m^2 s^{-1} (66.85 °C), respectively, enabling controlled heat distribution and limited rapid diffusion. The specific heat capacity (C_p) of the nanocomposites was measured at 36.85 °C, 56.85 °C, and 66.85 °C, representing body temperature and actuation conditions, to assess the impact of PPy@Fe_2O_3 NPs incorporation (Table S2, ESI†). Interestingly, C_p of the nanocomposite decreased with increasing content of PPy@Fe_2O_3 NPs, particularly from S0 to S10, indicating reduced thermal energy storage. While sample S15 showed a slight increase in C_p compared to S10, it remained lower than S0 across all measured temperatures. Generally, the incorporation of nanomaterials has a relatively limited impact on C_p of the nanocomposite. Take S5 at 56.85 °C as an example; with a specific heat capacity of 1.98 J g^{-1} K^{-1} (~5% decrease compared to S0), it maintains a balance between thermal stability and responsiveness, ensuring efficient heat absorption and rapid actuation under NIR irradiation.

To evaluate the feasibility of our 4D nanocomposites for biomedical applications, particularly in neural tissue engineering, we first assessed their biocompatibility with NE-4C NSCs. After seeding, the NSCs adhered to the substrates with 2–3 hours of incubation. After 24 hours, *via* a CCK-8 assay, the cells were observed on all substrates, including the tissue culture plate (TCP), and remained viable without any significant differences among groups. NSCs adopted their spread morphology with intact nuclei as identified by nuclei and F-actin staining. Besides, cells on all the substrates also proliferated over the culture period of 3 and 7 days, suggesting the material did not interfere with cell adhesion, viability, and proliferation (Fig. 4a and b). Previous studies from our lab have demonstrated the biocompatibility of BPD matrix, and PPy's biocompatibility is also well documented.[9,22,32,33] Another critical aspect of cellular behavior is cell differentiation. To evaluate this, NSCs were cultured in a neural differentiation medium for 10 days, and then analyzed by immunofluorescence staining for microtubule-associated protein 2 (MAP2). MAP2 is a key structural protein that stabilizes and organizes microtubules in dendrites, regulating the cytoskeleton to ensure proper neuronal morphology and support neurite outgrowth.[34,35] Thus, when maturing neurons undergo microtubule assembly, MAP2 expression marks a critical step in neurite formation.[36] The confocal microscopy images showed that NSCs cultured on both S0 and S5 substrates successfully differentiated, exhibiting MAP2 expression post-differentiation (Fig. 4c). These findings collectively suggest that, despite the high NP content in our nanocomposites, the materials exhibited excellent cytocompatibility.

Due to its effective NIR responsiveness, high mechanical strength, and support for cell growth, the 5% nanocomposite was selected for subsequent studies. However, one concern is that the heat generated from the photothermal effect during 4D transformation might lead to cell death on the 4D scaffold. To assess cell viability during transformation, various NIR illumination times were applied to the scaffold, with results shown in Fig. 4d. With increasing illumination time, a decrease in cell viability was observed. During the assessment, the heat generated by the photothermal effect dissipated quickly in the presence of the cell culture medium, resulting in a slower temperature increase in the cell viability study compared to the previous assessment, where the nanocomposite was directly exposed to NIR illumination. After 1 minute of illumination with 1000 mW NIR, the 4D scaffold reached approximately 42 °C, maintaining about 80% cell viability and ensuring sufficient cell numbers in the engineered tissue construct, which is consistent with our previous study.[22]

To further explore the biomedical application of our nanocomposite, we designed a 4D-printed semi-tubular structure with an aligned pattern, demonstrating its potential to control cellular behavior through 4D transformation. After printing,

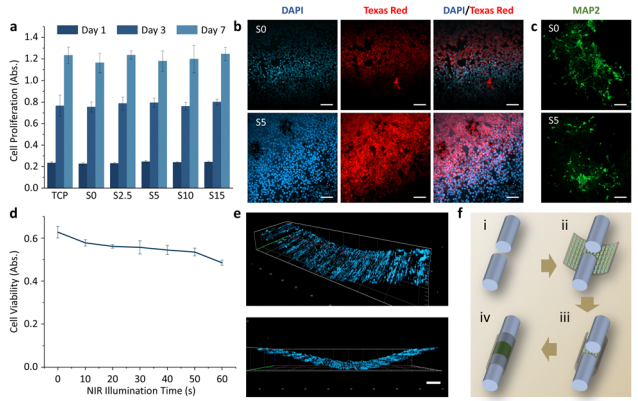

Fig. 4 NIR responsive 4D printed semi-tubular constructs. (a) Proliferation of NSC on 4D-printed scaffolds with different content of the NPs after 1, 3, and 7 days of culture. Data are reported as mean ± standard deviation, n = 6. (b) NSC morphology on pure SMP and nanocomposite (S5) scaffolds after 48 hours of culture, with F-actin colored red and the nucleus colored blue. No significant differences were observed among the samples, indicating that the PPy@Fe_2O_3 NPs-doped nanocomposites demonstrated excellent *in vitro* cytocompatibility. The scale bars are 200 μm. (c) Immunofluorescent images of NSC differentiation on 4D-printed scaffold prepared from pure SMP and nanocomposite containing 5% PPy@Fe_2O_3 NPs, respectively, after culturing in differentiation medium for 10 days. MAP2 is colored green. The scale bars are 200 μm. (d) NSC viability (absorption) measurement under different NIR illumination times. Data are reported as mean ± standard deviation, n = 6. (e) Distribution of NSCs on 4D printed semi-tubular structures after NIR-induced 4D transformation. The scale bar is 500 μm. (f) Schematic of the full tubulation of 4D nerve guidance conduit *via* a NIR-triggered shape transformation.

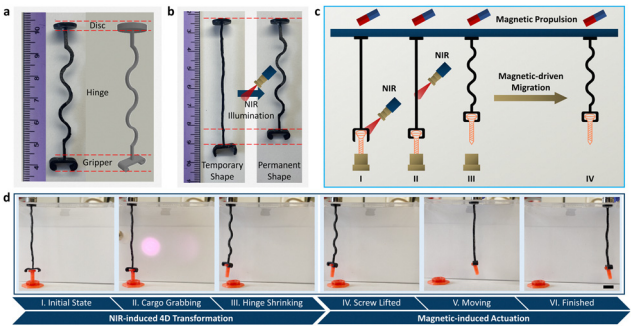

Fig. 5 4D-printed smart gripper whose operation, including grabbing, lifting, and movement, is actuated remotely by NIR illumination and an external magnetic field. (a) The 4D-printed smart gripper (left) and 3D model of it (right). (b) Under NIR illumination, the hinge segment can achieve a lift of 8 mm, and the grabber can achieve transformation from an open state to a closed state. (c) Schematic of the process of cargo delivery by the 4D-printed smart gripper *via* 4D transformation induced by NIR and magnetic field. (d) I and II, triggered by NIR illumination, the grabber part grabs the 3D-printed screw; III and IV, under NIR illumination, the hinge shrinks to its original shape, achieving an 8 mm lift; V and VI, driven by the external magnetic field, the gripper moves to the designated location, finished the delivery of the screw.

the semi-tubular construct was temporarily flattened. Then, NSCs were seeded onto the scaffold to ensure uniform distribution and cell survival post-photothermal transformation. After 1 day of culture, the cell-laden scaffold was exposed to mild NIR illumination to revert to its original 3D semi-tubular shape. Fig. 4e shows fluorescent images of NSC distribution on the 4D semi-tubular structure after NIR-induced 4D transformation. In addition, the aligned NSC distribution was also visible on the 4D construct. Previous studies showed that micro- or nanoscale topographical patterns can guide NSC alignment and enhance neurogenesis.[37,38] It demonstrates that our 4D-printed structures can control cell distribution both in 2D (aligned micropatterns) and 3D (semi-tubular shape) through 4D transformation, highlighting their potential in tissue engineering, particularly as nerve guidance conduits, as illustrated in Fig. 4f.

Grasping is a fundamental function of smart robots. 4D-printed smart robots are well-suited for achieving this through stimuli-responsive deformation. Leveraging the magnetic and NIR-responsive properties of our nanocomposite, we designed and fabricated a smart gripper capable of remotely grasping and delivering cargo. Fig. 5a shows the gripper, fully fabricated from the nanocomposite, with three key parts: a top disc for levitation and magnetic movement, a middle hinge for cargo lifting, and a bottom mechanical gripper for cargo grabbing. Under NIR illumination, the hinge achieved an 8 mm lift in a stepwise manner by transitioning from its temporary to its permanent shape, and meanwhile, the gripper transformed from an open state (temporary shape) to a closed, gripping state (permanent shape) (Fig. 5b). As shown in Fig. 5c, the delivery process is as follows: (I) under the first NIR illumination, the gripper grabs the cargo; (II) under the second NIR illumination, the hinge transforms from its extended state to a shrunk state, lifting the cargo; (III) and (IV) once the gripping and lifting processes are finished, the smart gripper moves toward the target spot, driven by the magnetic field. Our 4D-printed gripper successfully lifted a 0.4g 3D-printed screw and delivered it to the target location using remote NIR and magnetic control (Fig. 5d and Movie S4, ESI†). Similar 4D-printed smart grippers have also been reported in previous studies, achieving gripping through 4D transformations driven by strain mismatches or using alternative actuation methods, each with its own limitations. Typically, strain mismatch resulting from the anisotropic properties of a structure is achieved through a bi- or multi-layer design, created by using multiple materials or varying the fabrication process, which is often complex.[39,40] Compared to light-based actuation, which enables precise localized heating and remote dynamic control, other methods have various limitations. For example, grippers controlled by electric stimulation cannot be actuated remotely, and those actuated by direct heating lack precise, remote, and dynamic control.[41,42]

To further explore the application of our nanocomposite and inspired by crabs in nature, a smart robot—Smart Crab (SC)—was designed and fabricated to deliver cargoes and navigate a complex maze with precise remote control, as shown in Fig. 6a. SC was able to move with precise directional control, driven by an external magnetic field, due to its magnetic response properties. To demonstrate the precise propulsion of the magnetic SC, its trajectory was adjusted to trace the

pattern "GWU," showcasing its directional accuracy and cargo-carrying capabilities (Fig. 6b). As shown in Fig. 6c, both claws were heated with NIR illumination for manual cargo loading. Upon subsequent NIR exposure, the claws opened independently, releasing the cargoes through NIR-triggered 4D transformation, with each claw taking approximately 10 seconds to open. With magnetic response properties and NIR-induced 4D transformation, we hypothesized that SC could perform multiple cargo deliveries under remote control (Fig. 6d). To demonstrate the performance of the SC, a complex maze was created with two designated cargo release points, as shown in Fig. 6e: guided by a magnetic field, SC traveled from the start, releasing Cargo I at Spot 1 under NIR illumination, then continued to Spot 2, releasing Cargo II with another NIR activation, and exited the maze, completing the mission (Fig. 6f and Movie S5, ESI†). Although similar magnetic-driven robots have been reported, performing complex operations, such as delivering two different cargoes with remote and precise control, remains a challenge.[43] By leveraging the multi-responsive nanocomposite and 4D printing platform, we present a simple fabrication approach and successfully create a smart robot capable of executing precise, complex tasks.

Although the aforementioned 4D-printed SC can perform complex cargo deliveries *via* remote manipulation, 2D movement is often insufficient in real-life scenarios, as it does not account for the obstacles and complexities commonly encountered outside controlled lab environments. To address this need, a new smart robot, Smart Star (SS), was designed and fabricated, as shown in Fig. 7a and b, with the capability for three-dimensional movement and cargo delivery. Envisioning a biomedical scenario, we proposed using SS to deliver cell-laden hydrogel beads for repairing injured blood vessels *via* remote control. To replicate the tubular structure of blood vessels, a polyvinyl chloride tube with a 1.5 mm wall thickness was used, and alginate was selected to encapsulate NSCs, forming NSC-laden beads for cell protection.[44,45] As shown in Fig. 7c, an NSC-laden bead was loaded into SS in its closed temporary shape, and NIR illumination triggered SS to release the bead as it returned to its open shape. Additionally, the magnetic force from a ferromagnet could easily lift SS with a cell-laden alginate bead, establishing a foundational basis for 3D movement. To evaluate the effect of NIR-induced heating on cell viability within alginate beads, a live/dead assay was performed (Fig. 7d). By selectively irradiating the hinge region, heat generation was controlled, allowing most cells to survive the release process. As shown in Fig. 7e and Movie S6, ESI† SS transported an NSC-laden bead while navigating 3D movements within blood vessel structures, effectively avoiding obstacles under precise magnetic field control. Upon reaching the target site, NIR irradiation triggered the release of the cell beads, delivering them to

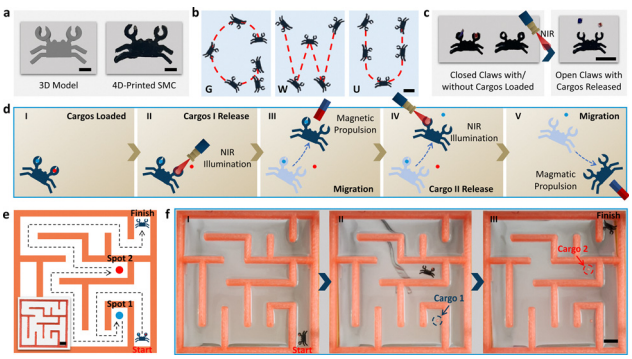

Fig. 6 Proof-of-concept smart robot – smart crab (SC) (a). The 3D model (left) and optical image of 4D printed SC (right). The scale bars are 2 mm. (b) Precise motion control of the SC to form a "GWU" pattern, driven by a magnetic field. Scale bar is 5 mm. (c) Optical images of SC show its claws in the closed state with and without cargo. Under NIR illumination, the claws transform into an open state and release cargo. The scale bar is 5 mm. (d) Schematic of cargo delivery of SMS: I, the cargoes are loaded into each of the claws manually; II, under NIR illumination, one of the claws opens, and cargo released; III, driven by the magnetic field, the SC can move to another location; IV, under the NIR illumination, the other claw opens, the other cargo released. V, driven by the magnetic field, the SC exits. (e) The maze was designed for the 4D printed SC to perform cargo delivery tasks and its optical image (inserted photo, the scale bar is 10 mm). (f) Controlled by NIR illumination and a magnetic field, the SC successfully delivered two cargoes to two different designated spots and then moved to the finish point. The scale bar is 10 mm.

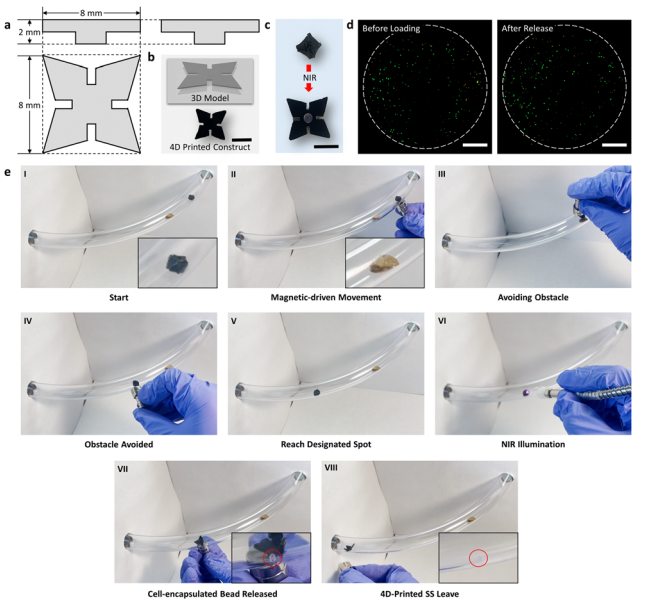

Fig. 7 Proof-of-concept Smart Star (SS). (a) The three-view drawing of SS. (b) The 3D model (up) and optical image (down) of 4D printed SS. The scale bar is 5 mm. (c) Under NIR illumination, the SS in the closed state (temporary shape) successfully transformed into the open state (permanent shape), completing the release of the alginate-encapsulated NSC bead. The scale bar is 5 mm. (d) Fluorescent images of NSC-encapsulated beads before and after NIR-induced release from SS. The scale bars are 200 μm. (e) Optical images of the SS delivering a cell bead in a simulated blood vessel: I, initially, the SS, loaded with NSCs-encapsulated bead is placed at the start position; II and III, driven by the magnetic field, the SS navigates over a preset obstacle, successfully avoiding it; IV and V, after avoiding the obstacle, the SS continues moving toward the assigned spot; VI and VII, under NIR illumination, the SS releases NSC-encapsulated bead at the designated location; VIII, after completing the delivery process, the SS departs. All the complex operations were completed through remote control.

the designated location. The process took approximately 15 seconds for all four arms to open and complete the release. This proof-of-concept demonstration of precise 3D navigation and controlled cell delivery highlights the versatility and potential of the 4D-printed SS and the nanocomposite for biomedical applications. Future advancements in material design, control systems, and size optimization could further expand its capabilities, supporting more complex *in vivo* tasks, such as targeted drug delivery and tissue repair.

Conclusion

In this study, an innovative multi-responsive 4D nanocomposite was successfully designed by doping synthesized NPs into a shape memory polymer matrix. It exhibits excellent photo- and magnetic-responsiveness. Compared to other 4D-printed materials, our nanocomposite enables precise, dynamical, and remotely controllable transformations in a spatiotemporal manner through NIR activation, and can move in 3D space *via* magnetic propulsion. Moreover, a proof-of-concept 4D printed semi-tubular construct was developed in this study, providing an efficient method for fabricating dynamic tissue constructs that fulfill both structural and functional requirements. Using our nanocomposite, three proof-of-concept smart robots were designed and fabricated for various purposes. Beyond basic cargo grabbing, these smart robots are capable of lifting, delivering two different cargoes to designated locations, and navigating in 3D space within confined environments. Importantly, all these complex operations are achieved through remote control using NIR illumination and an external magnetic field, highlighting the potential of our nanocomposite in various applications, such as cell or drug delivery for tissue repair or disease treatment. This research demonstrates that multi-responsive 4D printing, integrating remotely spatiotemporal capacities with nanomaterials, offers a promising strategy for future biomedical and versatile applications.

Materials and methods

Synthesis of Fe_2O_3@PPy nanoparticles

Fe_2O_3@PPy NPs were synthesized following a facile polymerization method as previously reported.[46] Briefly, 1 mL of pyrrole (Sigma Aldrich) and 2.74 g of *p*-toluenesulfonic acid monohydrate ($PTsOH{\cdot}H_2O$, Sigma-Aldrich) were added to 780 mL of deionized water and stirred for 30 minutes to obtain a homogeneous solution. Then, 1.2 g of Fe_2O_3 NPs (Alfa Aesar, 99.9% purity, size range of 20–40 nm) was added to the solution. Subsequently, 3.30 g of freshly prepared ammonium persulfate (Sigma-Aldrich), dissolved in 20 mL of deionized water, was added dropwise to the suspension to initiate pyrrole polymerization. The reaction was carried out for 60 minutes in a nitrogen environment and ice-cold conditions with constant stirring. Finally, the Fe_2O_3@PPy NPs were washed thoroughly with water first and then absolute ethanol using centrifugation to remove any traces of unreacted chemicals. The nanoparticle slurry was dried at 60 °C for 12 hours followed by mild grinding using a mortar pestle to obtain the workable nanoparticles. Post-synthesis, the NPs were characterized using Fourier transform infrared spectroscopy (Nicolet iS50, Thermo Scientific) within the wavenumber range of 4000–400 cm^{-1}.

Preparation of magnetoactive NIR-responsive 4D nanocomposite ink

The base formulation of the 4D ink consisted of three components: bisphenol A diglycidyl ether (BDE, monomer), poly(propylene glycol)bis(2-aminopropyl)ether (PBE, crosslinker), and decylamine (DA, crosslinking modulator), all purchased from Sigma-Aldrich. All three components were mixed homogeneously at room temperature in a molar ratio of 0.01 mol BDE, 0.00275 mol PBE, and 0.0045 mol DA *via* vortexing, followed by centrifugation at 1500 rpm for 3 minutes to remove air bubbles from the ink. In order to prepare magnetoactive NIR-responsive 4D inks, the synthesized Fe_2O_3@PPy NPs were added to the base formulation at different concentrations (0%, 2.5%, 5.0%, 10.0%, and 15%, w/w), generating the nanocomposites. The nanocomposite inks were homogenized by 5 minutes of mechanical stirring, followed by 10 minutes of sonication, before being set aside for further use. The 4D inks (base formulation) were used as a control in the study.

Fabrication of the magnetoactive NIR-responsive 4D constructs

In our study, two different fabrication strategies, FDM and mold casting, were combined to fabricate the 4D constructs. Firstly, the 3D master molds were designed using the software Autodesk123D (Autodesk Inc.) and the.stl format file was processed using GrabCAD Print (Stratasys Inc.) software. The master molds were printed using an FDM printer (Stratasys F370) with acrylonitrile styrene acrylate (ASA) filaments (Stratasys Inc.). The printing parameters included slice height (0.01 inch), and infill style (sparse-high density) while keeping the remaining parameters as default. Subsequently, replica molds were prepared using polydimethylsiloxane (PDMS) as reported previously.[9] Next, a preset amount of the 4D nanocomposite ink was extruded into the PDMS mold, degassed, and cured at 75 °C overnight for polymerization. The samples were then harvested from the molds and used further. All the constructs referenced in this research, including the flower, butterfly, human figure, semi-tubular structure, smart gripper, SC, and SS, were prepared using S5 ink following this method. Notably, the samples prepared for biological characterization were immersed in dH_2O for at least 3 days to leach out any residual unreacted chemicals.

Physicochemical and mechanical characterization

Morphological analysis of the synthesized Fe_2O_3@PPy NPs and 4D samples was performed by an FEI high-resolution Teneo LV SEM (Thermo Scientific) under an accelerating voltage of 2 kV. Prior to visualization, the samples were sputter-coated with gold (2 nm thickness). In addition, the elemental composition of Fe_2O_3@PPy NPs was characterized using SEM coupled with Energy-dispersive X-ray spectroscopy (EDX, EDAX Octane Pro,

AMETEK). The samples were prepared by dispersing a small amount of dried powder onto conductive carbon tape adhered to an aluminum SEM stub, without any coating. Point analysis and elemental mapping were conducted to confirm the presence and distribution of Fe, O, C, and N.

To measure the glass transition temperature (T_g), sample pellets with dimensions of 5 mm × 3 mm (D × H) were loaded into a multi-cell differential scanning calorimeter (MC-DSC, TA Instruments). The samples were subjected to two heating–cooling cycles within a temperature range of 0–150 °C with a programmed ramp rate of 1 °C minute^{-1}. The T_g was determined from the second cycle using NanoAnalyze (TA Instruments).

Thermal conductivity was measured using the comparative cut bar technique, a well-established steady-state method for thermal analysis.[47] Samples measuring 15 mm × 3 mm (D × H) were positioned upon a standard aluminum (Al) cylinder measuring 15 mm × 5 mm (D × H) with a known thermal conductivity value of 200.0 W m^{-1} K^{-1}.[48] A heating plate served as the heat source, providing a consistent heat flow through the Al cylinder, while ice water acted as the heat sink, maintaining a stable temperature difference between the heat source and the sink. To eliminate air gaps, a thin layer of thermal paste was applied between the sample and Al blocks. Temperature distribution along the heat flow direction was recorded using 4-channel thermocouple thermometer (Landtek). The difference of temperature across the Al cylinder was recorded as ΔT_2, and the difference of temperature across the samples was recorded as ΔT_1. Besides, the cross-sectional areas of the Al cylinder and the samples were recorded as A_2 and A_1, respectively. While the thicknesses of the Al cylinder and the samples were recorded L_2 and L_1, respectively. The thermal conductivity of sample (K_s) was determined using the following equation, in which K_{Al} is thermal conductivity of Al:

$$K_s = K_{Al}\frac{A_2 \times \Delta T_2 \times L_1}{A_1 \times \Delta T_1 \times L_2}$$

The specific heat capacity of the samples was characterized using the same MC-DSC instrument with synthesized sapphire (SRM720, NIST) as the reference material. The experiment was conducted in three sequential steps: (i) baseline measurement with empty crucibles, (ii) reference measurement using the sapphire, and (iii) sample measurement. All measurements were subjected to two heating–cooling cycles within a temperature range of 0–150 °C at a programmed ramp rate of 1 °C minute^{-1}. The heat flow data obtained from the DSC scans were processed using NanoAnalyze. The specific heat capacity of the samples ($C_{p,sample}$) was calculated based on the ratio of the heat flow of the sample to that of the sapphire reference at different temperatures, following the equation:

$$C_{p,sample} = C_{p,reference}\frac{(Y_{sample} - Y_{baseline}) \times m_{reference}}{(Y_{reference} - Y_{baseline}) \times m_{sample}}$$

where Y_{sample}, $Y_{reference}$, and $Y_{baseline}$ represent the heat flow signals of the sample, reference (sapphire), and baseline at difference temperature, respectively. Similarly, m_{sample} and $m_{reference}$ denote the masses of the sample and reference (sapphire), respectively.

Thermal diffusivity was calculated based on the thermal conductivity and specific heat capacity of the samples following the equation:

$$\alpha = \frac{k}{\rho \times C_p}$$

where α, k, ρ, and C_p represent the thermal diffusivity, thermal conductivity, density, and specific heat capacity of the material, respectively.

Tensile testing was performed using an electromechanical universal test system (MTS Criterion Model 43). In brief, samples with dimensions of 20 mm × 10 mm × 1 mm ($L \times W \times H$) were mounted on the 5 kN load cell. Before the tensile measurement was taken, the preload was set to 0.01 N. The measurements were performed at a speed of 1 mm minute^{-1} until breakpoints. Data were collected using TW Elite software (MTS Systems), and the tensile modulus was calculated by the linear portion of the tensile stress–strain curve.

Characterization of shape memory properties

Shape memory tests were performed following the method reported in our previous research.[9] Briefly, at 60 °C, strips with dimensions of 70 mm × 10 mm × 1 mm ($L \times W \times H$) were bent into a ''U'' shape with an inner diameter of 10 mm with the assistance of a custom-made ''U''-shape device and immediately placed in ice water for shape fixation. The fixed angle of the samples was determined and recorded as ϑ_{fixed}. The strips were then immersed in a water bath, preset to a specific temperature and their shape recovery was recorded using iPhone 12 Pro Max (Apple Inc.). The final angle of the samples was recorded as ϑ_{final}. Shape fixation and shape recovery properties of the sample were measured by shape fixation ratio (R_f) and shape recovery ratio (R_r), respectively, and they were determined by the following equations:

$$R_f = \vartheta_{fixed}/180 \times 100\%$$

$$R_r = (\vartheta_{fixed} - \vartheta_{final})/\vartheta_{fixed} \times 100\%.$$

For testing the NIR-responsive properties, the ''U''-shaped samples (as mentioned above) were subjected to an NIR laser (808 nm), keeping the distance between the sample and laser fixed at 5 cm. The recovery process was captured using an iPhone 12 (Apple Inc.) and the time to achieve NIR-induced 90° angle recovery was recorded.

Biological characterization

Mouse neuroectoderm-derived NSCs (NE-4C) were obtained from the American Type Culture Collection (ATCC). NSCs (passage numbers 3–6) were cultured in Minimum Essential Medium Eagle (Sigma-Aldrich) supplemented with 5% (v/v) fetal bovine serum (FBS) and 1% penicillin/streptomycin solution. All cells were incubated under standard cell culture

conditions of 37 °C in a humidified environment with 5% CO_2 and 95% humidity.

Cell proliferation on the scaffold was evaluated using a CCK-8 assay after 1, 3, and 7 days of culture. Before cell seeding, all samples were sterilized with 70% ethanol, followed by multiple washes with phosphate-buffered saline (PBS, Corning Inc.) and two washes with cell culture medium. Throughout the study, scaffolds were seeded with NSCs at a fixed density of 3×10^3 cells per scaffold. At predetermined intervals, the culture medium containing 10% CCK-8 solution (Dojindo) was added and incubated for 2 hours. After incubation, 100 μL of the medium was transferred into another 96-well plate, and absorbance at a wavelength of 450 nm was quantified using a spectrophotometer (Thermo Scientific).

For cell morphology analysis, cell-laden scaffolds were fixed using 10% neutral buffered formalin for 10 minutes, followed by permeabilization with 0.2% Triton X-100 for 10 minutes. The cell-laden scaffolds were stained with a Texas Red-X phalloidin solution (1 : 400) for 20 minutes to visualize F-actin, followed by a 4′,6-diamidino-2-phenylindole (DAPI) (1 : 1000) solution for another 5 minutes to label nuclei. NSC morphology on the scaffolds was subsequently imaged using confocal microscopy for detailed structural analysis (Carl Zeiss).

For neuronal differentiation studies, NSC-seeded scaffolds were subjected to a complete cell culture medium supplemented with 5×10^{-5} M all-trans retinoic acid (RA) for 10 days. Thereafter, the samples were fixed with 10% neutral buffered formalin for 15 minutes, then permeabilized in 0.2% Triton X-100 solution for 10 minutes at room temperature. Subsequently, the samples were incubated with a blocking solution comprising 1% bovine serum albumin, 0.1% Tween 20, and 0.3 M glycine in PBS for 2 hours. The samples were incubated with rabbit anti-MAP2 primary antibody (1 : 500 in PBST) overnight at 4 °C, followed by incubation in goat anti-rabbit Alexa Fluor 488 secondary antibody (1 : 1000 in PBST) for 2 hours at room temperature. The nuclei were stained with DAPI (1 : 1000). The immunofluorescence images were taken using confocal microscopy (Carl Zeiss).

To prepare NSC-encapsulated alginate beads, a 3% sodium alginate (Sigma-Aldrich) solution was prepared by dissolving it in normal saline under constant stirring. NSCs were then added at a density of 3×10^7 cells per mL, and the solution was gently pipetted to ensure even cell distribution. To crosslink the beads, the sodium alginate solution with NSCs was dripped into a 2% $CaCl_2$ solution in a drop-by-drop manner for crosslinking as reported previously elsewhere.[49] The crosslinked beads were then washed three times with cell culture medium for further use. To assess cell viability before and after delivery, the Live/Dead Cell Staining Kit (Abcam Inc.) was used according to the manufacturer's instructions, and the stained cells were subsequently imaged using a confocal microscope (Carl Zeiss).

Author contributions

Shengbo Guo: conceptualization, investigation, methodology, formal analysis, writing – original draft. Tarun Agarwal: conceptualization, investigation, methodology, writing – review & editing. Shuaiqi Song: investigation, validation. Kausik Sarkar: writing – review & editing. Lijie Grace Zhang: conceptualization, supervision, funding acquisition, writing – review & editing.

Data availability

The data supporting this article have been included as part of the ESI.†

Conflicts of interest

The authors declare no conflict of interest.

Acknowledgements

The authors would like to thank the financial support provided by NSF AM program grant 2427645 and EMBS program grant 2110842. We gratefully acknowledge Prof. Xinran Zhang from the Institute for Soft Matter Synthesis and Metrology at Georgetown University for his kind help with DSC characterization. In addition, we gratefully acknowledge Department of Chemistry from Columbian College of Arts & Sciences at the George Washington University for their kind help with FTIR characterization.

References

1 Y. Wang, H. Cui, T. Esworthy, D. Mei, Y. Wang and L. G. Zhang, *Adv. Mater.*, 2022, **34**, 2109198.
2 S. Miao, N. Castro, M. Nowicki, L. Xia, H. Cui, X. Zhou, W. Zhu, S.-J. Lee, K. Sarkar, G. Vozzi, Y. Tabata, J. Fisher and L. G. Zhang, *Mater. Today*, 2017, **20**, 577–591.
3 T. Agarwal, S. Y. Hann, I. Chiesa, H. Cui, N. Celikkin, S. Micalizzi, A. Barbetta, M. Costantini, T. Esworthy and L. G. Zhang, *J. Mater. Chem. B*, 2021, **9**, 7608–7632.
4 S. Y. Hann, H. Cui, M. Nowicki and L. G. Zhang, *Addit. Manuf.*, 2020, **36**, 101567.
5 S. Guo, H. Cui, T. Agarwal and L. G. Zhang, *Small*, 2024, **20**, 2307750.
6 A. Y. Lee, J. An and C. K. Chua, *Engineering*, 2017, **3**, 663–674.
7 X. Xiao, D. Kong, X. Qiu, W. Zhang, F. Zhang, L. Liu, Y. Liu, S. Zhang, Y. Hu and J. Leng, *Macromolecules*, 2015, **48**, 3582–3589.
8 K. Shahi and V. Ramachandran, *Polymers*, 2022, **14**, 2753.
9 S. Miao, H. Cui, T. Esworthy, B. Mahadik, S. J. Lee, X. Zhou, S. Y. Hann, J. P. Fisher and L. G. Zhang, *Adv. Sci.*, 2020, **7**, 1902403.
10 X. Kuang, K. Chen, C. K. Dunn, J. Wu, V. C. Li and H. J. Qi, *ACS Appl. Mater. Interfaces*, 2018, **10**, 7381–7388.
11 G. Chen, B. Jin, Y. Shi, Q. Zhao, Y. Shen and T. Xie, *Adv. Mater.*, 2022, **34**, 2201679.
12 H. Yang, W. R. Leow, T. Wang, J. Wang, J. Yu, K. He, D. Qi, C. Wan and X. Chen, *Adv. Mater.*, 2017, **29**, 1701627.
13 C. Xin, D. Jin, Y. Hu, L. Yang, R. Li, L. Wang, Z. Ren, D. Wang, S. Ji, K. Hu, D. Pan, H. Wu, W. Zhu, Z. Shen,

Y. Wang, J. Li, L. Zhang, D. Wu and J. Chu, *ACS Nano*, 2021, **15**, 18048–18059.
14 M. Chen, X. Fang, S. Tang and N. Zheng, *Chem. Commun.*, 2012, **48**, 8934–8936.
15 X. Wang, X. Gu, C. Yuan, S. Chen, P. Zhang, T. Zhang, J. Yao, F. Chen and G. Chen, *J. Biomed. Mater. Res., Part A*, 2004, **68**, 411–422.
16 S. Majumdar, J. Nath and D. Mahanta, *J. Environ. Chem. Eng.*, 2018, **6**, 2588–2596.
17 A. Pandiyarajan, S. Venkateshbabu, G. Sarojini, R. Natarajan and R. Manivasagan, *Waste Biomass Valorization*, 2023, **15**, 1–18.
18 J. B. Leach, J. B. Wolinsky, P. J. Stone and J. Y. Wong, *Acta Biomater.*, 2005, **1**, 155–164.
19 J.-E. Ehlers, N. G. Rondan, L. K. Huynh, H. Pham, M. Marks and T. N. Truong, *Macromolecules*, 2007, **40**, 4370–4377.
20 R. Thomas, C. Sinturel, S. Thomas and E. M. Sadek El Akiaby, *Micro-Nanostruct. Epoxy/Rubber Blends*, 2014, 1–30, DOI: 10.1002/9783527666874.ch1.
21 S. M. Hasan, G. Harmon, F. Zhou, J. E. Raymond, T. P. Gustafson, T. S. Wilson and D. J. Maitland, *Polym. Adv. Technol.*, 2016, **27**, 195–203.
22 H. Cui, S. Miao, T. Esworthy, S.-J. Lee, X. Zhou, S. Y. Hann, T. J. Webster, B. T. Harris and L. G. Zhang, *Nano Res.*, 2019, **12**, 1381–1388.
23 P. P. Vijayan, in *Shape Memory Polymers, Blends and Composites: Advances and Applications*, ed. J. Parameswaranpillai, S. Siengchin, J. J. George and S. Jose, Springer, Singapore, 2020, pp. 199–217, DOI: 10.1007/978-981-13-8574-2_9.
24 L. Yang, J. Lou, J. Yuan and J. Deng, *RSC Adv.*, 2021, **11**, 28838–28850.
25 C.-S. Yun, J. S. Sohn and S. W. Cha, *Polymers*, 2020, **12**, 351.
26 M. ElMaoud, W. Abuzaid and M. Alkhader, *Polymer*, 2022, **248**, 124812.
27 M. Wei, Y. Zhu, X. Wang, X. Ma, H. Ma, Y. Du, R. Chen, J. Ji and M. Xue, *Adv. Funct. Mater.*, 2024, **34**, 2316255.
28 C. Liu, H. Qin and P. Mather, *J. Mater. Chem.*, 2007, **17**, 1543–1558.
29 Z. Said, A. K. Pandey, A. K. Tiwari, B. Kalidasan, F. Jamil, A. K. Thakur, V. V. Tyagi, A. Sarı and H. M. Ali, *Prog. Energy Combust. Sci.*, 2024, **104**, 101162.
30 Y. Xie and X. Wang, *Green Carbon*, 2023, **1**, 47–57.
31 J. Gao, in *Handbook of Liquid Metals*, ed. J. Liu and W. Rao, Springer Nature, Singapore, 2024, pp. 1–39, DOI: 10.1007/978-981-19-2797-3_26-1.
32 F. Villanueva-Flores, I. Garcia-Atutxa, A. Santos and J. Armendariz-Borunda, *Pharmaceutics*, 2023, **15**, 1750.
33 E. Stewart, N. R. Kobayashi, M. J. Higgins, A. F. Quigley, S. Jamali, S. E. Moulton, R. M. Kapsa, G. G. Wallace and J. M. Crook, *Tissue Eng., Part C*, 2015, **21**, 385–393.
34 J. H. Dinsmore and F. Solomon, *Cell*, 1991, **64**, 817–826.
35 J. H. Morrison, P. R. Hof and G. W. Huntley, in *Handbook of Chemical Neuroanatomy*, ed. F. E. Bloom, A. Björklund and T. Hökfelt, Elsevier, 1998, vol. 14, pp. 299–430.
36 X. Zhou, H. Cui, M. Nowicki, S. Miao, S.-J. Lee, F. Masood, B. T. Harris and L. G. Zhang, *ACS Appl. Mater. Interfaces*, 2018, **10**, 8993–9001.
37 L. Vaysse, A. Beduer, J. Sol, C. Vieu and I. Loubinoux, *Biomaterials*, 2015, **58**, 46–53.
38 S. H. Lim, X. Y. Liu, H. Song, K. J. Yarema and H.-Q. Mao, *Biomaterials*, 2010, **31**, 9031–9039.
39 C. Yoon, R. Xiao, J. Park, J. Cha, T. D. Nguyen and D. H. Gracias, *Smart Mater. Struct.*, 2014, **23**, 094008.
40 Y. Zou, Z. Huang, X. Li and P. Lv, *Front. Mater.*, 2021, **8**, 661999.
41 H. Wei, X. Cauchy, I. O. Navas, Y. Abderrafai, K. Chizari, U. Sundararaj, Y. Liu, J. Leng and D. Therriault, *ACS Appl. Mater. Interfaces*, 2019, **11**, 24523–24532.
42 C. Cui, L. An, Z. Zhang, M. Ji, K. Chen, Y. Yang, Q. Su, F. Wang, Y. Cheng and Y. Zhang, *Adv. Funct. Mater.*, 2022, **32**, 2203720.
43 C. Xin, D. Jin, R. Li, D. Wang, Z. Ren, B. Liu, C. Chen, L. Li, S. Liu, B. Xu, Y. Zhang, Y. Hu, J. Li, L. Zhang, D. Wu and J. Chu, *Small*, 2022, **18**, 2202272.
44 J. Lai, A. K. Azad, W. M. A. W. Sulaiman, V. Kumarasamy, V. Subramaniyan and S. A. Alshehade, *Pharmaceutics*, 2024, **16**, 370.
45 C. Colin, E. Akpo, A. Perrin, D. Cornu and J. Cambedouzou, *Molecules*, 2024, **29**, 2515.
46 K. Le, M. Gao, D. Xu, Z. Wang, G. Wang, W. Liu, F. Wang and J. Liu, *Dalton Trans.*, 2020, **49**, 9701–9709.
47 D. Zhao, X. Qian, X. Gu, S. A. Jajja and R. Yang, *J. Electron. Packag.*, 2016, **138**, 040802.
48 Y. Chen, Z. Gao, S. A. Hoo, V. Tipnis, R. Wang, I. Mitevski, D. Hitchcock, K. L. Simmons, Y.-P. Sun, M. Sarntinoranont and Y. Huang, *Adv. Mater.*, 2024, **36**, 2314097.
49 S. Kulanthaivel, S. Rathnam, T. Agarwal, S. Pradhan, K. Pal, S. Giri, T. K. Maiti and I. Banerjee, *J. Mater. Chem. B*, 2017, **5**, 4177–4189.